Study of Fiber-Based Wearable Energy Systems

Xiaoming Tao

Research Centre for Smart Wearable Technology, Institute of Textiles and Clothing, The Hong Kong Polytechnic University, Hong Kong, China

CONSPECTUS

Fiber-based electronic and photonic devices have the most desired human-friendly features, such as being soft, ubiquitous, flexible, stretchable, light, and permeable, and thus are ideal to be employed as the interface platform between humans, the environment, and machines. Today, these smart wearable devices are normally powered by rechargeable batteries. It is extremely desirable to have an undisrupted power supply for us to go anywhere at any time. Harvesting energy from the ambient environment or our body can potentially fulfill such a goal. Explorations of high performance, flexible functional materials and energy conversion devices have led many exiting discoveries. In order to realize their applications, equally important are fundamental studies of the physical phenomena and mechanisms that will provide scientific guidance for the direction of exploration and development of devices and systems. Hence, this Account provides a brief review of our recent progress in this topic area.

Based upon materials science, mechanics and device physics, we have succeeded in establishment of several new theoretical models for fiber-based piezoelectric, triboelectric, and hybrid generators. These models have been verified experimentally. Excellent results were obtained for fiber-based triboelectric generators without any adjustable parameters. Reasonable agreement was demonstrated for the piezoelectric generators because of some uncertainty in the material properties and deformation modes. From both simulated and experimental results, we did not detect any synergic effect in the hybrid generator consisting of cascaded piezoelectric and triboelectric units. The verified models can be used to predict the output voltage, current, and power of the devices in terms of material properties, parameters of device structure, harvesting circuits, and operating conditions. Furthermore, by considering the electric breakdown due to field-induced-emission and gas-ionization, we have identified the theoretical upper limits of charge density and output power from contact-mode fiber-based triboelectric nanogenerators. The analysis sheds new light on the scope and focus for further exploration and provides guidance on engineering design of such devices. In addition, we have setup an experimental platform for reliable triboelectric charge measurement of highly deformable and porous materials like fabrics. An extended triboelectric series has been reported by us including 21 types of commercial and new fibers. Based upon the findings, we have made significant improvements of the performance of these energy harvesting devices.

Finally, we have explored a class of new flexible thermoelectric materials exhibiting high performance for fiber-based thermoelectric generators, which can be fabricated by low-temperature

and cost-effective processes, such as in situ reduction coating and three-dimensional printing. The resultant large-area, flexible, and wearable fiber-base thermoelectric generators are key devices for great potential applications such as powering wearable microelectronic systems, active microclimate regulating systems, and waste thermal energy harvesting.

1. INTRODUCTION

Fiber-based electronic and photonic devices are soft, ubiquitous, flexible, stretchable, light, and permeable, having the most desired human-friendly features, and thus are ideal to be used for the interface platform between humans and machines, as well as body area network.1,2 In recent years, they have been extensively investigated by our group, including highly durable large strain sensors3−5 (up to 60% strain and over 1 million loading cycles), medium to high pressure (50 kPa to 10 MPa) sensors,6−8 fiber optic sensors9 for simultaneous measurement of a few kilopascal pressure and shear force at the human and clothing interface, temperature sensors and sensing networks,10−12 humidity sensors,13 gas sensors,14,15 highly durable and 3D deformable fabric circuit boards,16 light-emitting devices,17−19 and actuators,20,21 among others. These devices have been further investigated for a range of wearable applications including an intelligent footwear system for continuous monitoring of planar pressure distributions,22,23 a monitoring system of contractility of skeletal muscles in motion,24−26 compression garments,27 respiration monitoring,28 phototherapy,17,18 supercapacitors,29−33 self-powered sensors, 34 and so on. The study has contributed to the launch of a number of smart wearable systems in the market: to name a few, intelligent insoles, footwear, and training systems for relaxation for sleep therapy and pregnant women.

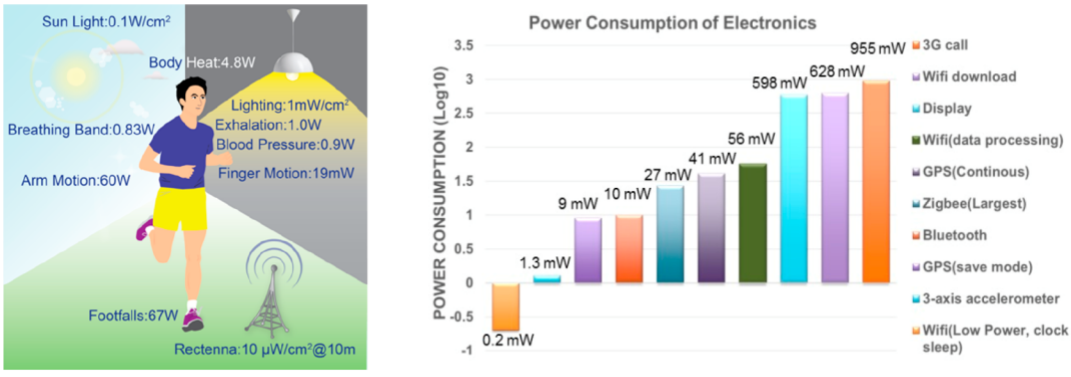

(a) (b)

Figure 1. (a) Possible energy sources. (b) Power consumption of microelectronic devices.

These smart wearable systems normally comprise a sensing network, modules for communication and data processing, and a power supply in the tens of milliwatts in the form of rechargeable batteries. It is extremely desirable that harvested energy from the ambient environment or our body can replace the batteries or prolong their life so that the wearable systems can work for us anywhere at any time. The energy available to be harvested, as illustrated in Figure 1a, is much higher than that required by all the modern microelectronic devices shown in Figure 1b. However, the energy sources available are not continuous; for instance, photovoltaic cells work well in the sun but not at night, and in cities, most people stay indoors where the light power density is much less than that outdoors in the sun. As such, a single source energy harvesting system is often intermittent and unpredictable in terms of power generated; thus we have to develop multiple-sourced energy systems for many of the intended applications. This Account provides a brief and timely review of our recent endeavors on this topic including fundamental theories, materials synthesis, device design and fabrication technologies, and the related harvesting circuits.

2. FIBER-BASED PIEZOELECTRIC NANOGENERATOR (FPENG)

FPENGs directly convert mechanical energy into usable electric energy with the ease of integration into a system. When an external force is applied to the piezoelectric material, the stress-induced deformation of the dipole generates electric charges. The charges generated on the surface can be transferred and collected by harvesting circuits. Since the fiber assemblies or textiles are soft, flexible, and deformable in three dimensions, they are highly desirable as wearable piezoelectric devices. However, the stress level in such fiber assemblies is low as the slender fibers are bent instead of stretched or compressed, which hinders the piezoelectric effects. Furthermore, the internal architecture and surface effect of the fabric result in complex deformation modes. Because fibrous structures allow low-stress operation and arrest the rapid propagation of cracks or damage, outstanding fatigue resistance and damage tolerance are the most noticeable features of fiber-based devices. Our investigations have been focused on these aspects.

2.1. Highly Durable All-fiber FPENG

Figure 2a illustrates a FPENG with a sandwich structure,35 which comprises an elastic conductive knitted fabric as the top and bottom electrodes and a polyvinylidene difluoride (PVDF)/NaNbO3 nanofiber nonwoven fabric as an active piezoelectric element. NaNbO3 nanowires were fully dispersed within the PVDF matrix to form a composite nanofiber with a core−sheath architecture (Figure 2b). The transformation from α-phase to β-phase crystalline in the as-spun PVDF fibers was evident by XRD due to the nanoconfinement and seeding effect for crystallization of NaNbO3 nanowires. The electrode fabrics were knitted with a composite yarn in which highly stretchable segmented polyurethane yarns were the core, helically wrapped with silver coated polyamide yarns as the sheath (Figure 2c). During cyclic compression tests, the FPENG exhibits large deformation as illustrated by Figure 2d,e.

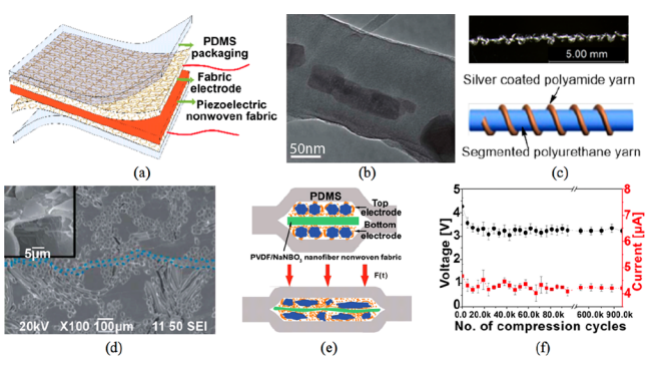

Figure 2. (a) Schematic of all-fiber FPENG. (b) SEM micrograph of PVDF/NaNbO3 nanofibers. (c) Images of composite yarn. (d) SEM micrograph of deformed cross-section of FPENG. (e) Schematics of the undeformed and deformed FPENG. (f) Output voltage and current of FPENG vs compression cycles. Reproduced with permission from ref 35. Copyright 2013 Royal Society of Chemistry.

Most noticeably, the FPENG maintains its performance after 1 000 000 compression cycles (Figure 2f), while the control with aluminum foil electrodes fail very quickly. This has been the highest number reported in the literature. The fibrous structure facilitates significant reduction in fiber strain and blockage of damage propagation thus providing an excellent solution for the poor durability of wearable energy harvesters.

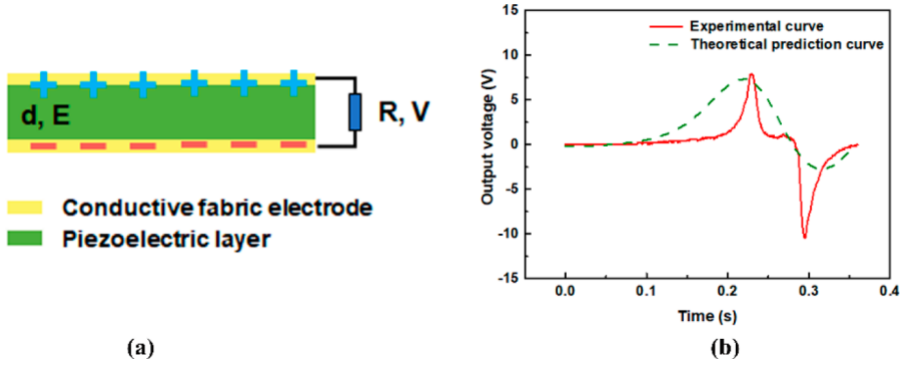

Figure 3. (a) Schematic illustration of FPENG. (b) Comparison between theoretical and experimental results. Reproduced with permission from ref 37. Copyright 2018 Royal Society of Chemistry.

Due to the porous and flexible structures, the deformation under compression in the sandwich generator is rather complex. Hence, the charges are generated from the compressive strain of the PVDF/NaNbO3 nanofiber in d33 and d31 modes, which is not desirable as it will cancel out the surface charges. Additionally, the uneven surficial morphology of the fabric can induce the in-plane membrane stretching or compression within the piezoelectric fabric by friction. Last, flexoelectric effects may arise in these nonuniformly deformed areas inside the nonwoven fabric, where freely deformed nanofibers give rise to the strain gradient within the piezoelectric fabric. As a result, a low peak output voltage of 3.4 V was obtained in a cyclic compressive test at 1 Hz and 0.2 MPa maximum pressure (Figure 2f). This study of FPENG highlights the need for theoretical models to guide device design and construction on a solid scientific basis.

2.2. Theoretical Analytical Framework for FPENG

The piezoelectric charges induced by stress or strain will determine the output performance of the generators. In an attempt to link the output performance with the material properties and fibrous structure, a theoretical framework was proposed based on the materials' constituent relationship and strain field.36 Since both the length and width of the piezoelectric layer are several orders of magnitude larger than its thickness (Figure 3a), d, the electric field, E, can be calculated by Gauss's law

$$E = -\frac{\sigma(t)}{\varepsilon_0\,\varepsilon_r} \quad (1)$$

where σ(t) presents the surface charge density of the electrode and ε_0 and ε_r are the air permittivity and relative permittivity of the piezoelectric material. Moreover, the electric potentials in the close loop circuit should follow

$$Ed + V = 0 \quad (2)$$

According to Ohm's law, the output voltage is a function of resistance, R, as

$$V = RI = R\frac{dQ}{dt} \quad (3)$$

Combing eqs 1−3, the amount of charges, Q, is given by

$$R\frac{dQ}{dt} + \frac{Q}{S}\frac{d}{\varepsilon_0\,\varepsilon_r} = 0 \quad (4)$$

On one hand, Q is determined from the constitutional relationship

$$Q(t) = d_{31} Y_c w s_1(t) + d_{33} Y_c w l s_3(t) \quad (5)$$

where d_{31} and d_{33} are the piezoelectric constants in the vertical and horizontal directions, s_1 and s_3 are the strain components in the piezoelectric layer, and Y_c, l, and w are the thickness, length, and width of the piezoelectric layer, respectively.

The expression in eq 5 has taken into consideration the strain distribution in fibrous structures and piezoelectric working modes; therefore, the above framework is applicable for most textile structures in a unit-cell approach since their repeat units are defined.

The above analysis does not include the time-related and strain-gradient effects of the piezoelectric materials. In practice, the time or strain-gradient-related constitutional relationships are poorly defined, and loading history is often unknown. Alternatively, one may directly solve eq 4 with the initial transferred charges37 below. The values from calculation and experiments agree reasonably, although the calculated curve may have a slightly different shape, as shown in Figure 3b.

$$Q(t) = Q_0 \, exp\left(-\int_0^t \frac{d_0 - x(\tau)}{RS\varepsilon_r\varepsilon_0} d\tau\right) \quad (6)$$

the surface, initial thickness, and movement of the upper surface. Hence, replacing eq 6 into eqs 3 and 4, the output current and voltage are

$$\begin{cases} I(t) = \dfrac{dQ(t)}{dt} = -\dfrac{(d_0 - x(t))Q_0}{RS\varepsilon_r\varepsilon_0} \, e^{-\int_0^t d_0 - x(\tau)/RS\varepsilon_r\varepsilon_0 \, d\tau} \\ V(t) = RI(t) = -\dfrac{(d_0 - x(t))Q_0}{S\varepsilon_r\varepsilon_0} \, e^{-\int_0^t d_0 - x(\tau)/RS\varepsilon_r\varepsilon_0 \, d\tau} \end{cases} \quad (7)$$

2.3. Enhancement of FPENG Output Performance

Significant improvement was demonstrated by raising the strain via introducing $BaTiO_3$ microparticles into PVDF nanofiber mat.37 The FPENG has a three-layer sandwich structure with a woven fabric electrode and a PVDF/CNT/ $BaTiO_3$ fiber mat. Its rectified output voltage peak reached 23 V, 10 times higher than the previous FPENG.36 The enhanced mechanism of this FPENG is mainly attributed to the BaTiO3 microparticles. First, the inorganic non-centrosymmetric particles have higher piezoelectric constants than polymers.

Second, the Young's modulus of PVDF fabric is 38 MPa, much smaller than the 168 MPa of the microparticles; the squeeze between BaTiO3 microparticles or microparticles and PVDF nanofibers leads to larger strain or strain gradient in the polarized PVDF nanofibers.

Alternatively, the output performance of FPENG was improved by adding conductive Ag nanowire in P(VDF− trifluoroethylene (TrFE)) nanofibers.36 Very high output voltage of 247.8 V and

current of 31.6 μA were demonstrated, due to the induced larger contact surfaces of nanowires, higher strain, or strain gradients.

3. FIBER-BASED TRIBOELECTRIC NANOGENERATOR (FTENG)

Since the first report by Wang in 2014,38 FTENGs have been explored to harvest mechanical energy, taking advantage of electrostatic induction and triboelectrification.39−41 To date, the time-average power output from wearable TENG systems has reached microwatts per square centimeter, still several orders of magnitude away for most real applications of microelectronic wearable systems in the milliwatt range. Hence, enhancement of power output is extremely crucial for the intended applications. Meanwhile, the triboelectrification mechanism in FTENGs remained largely elusive. One would naturally ask: How does the FTENG work? Can we predict its output performance based on the materials properties, device structure, and operation conditions? How much further improvement can be made, to milliwatt or even bigger? What is the theoretical upper limit of the output from a given FTENG and operational conditions?

We have conducted both theoretical and experimental investigations in order to answer these queries. First, a fully verified theoretical work has been established, which can be applied to illustrate the working mechanism and predict the performance of FTENGs in terms of material properties, device structures, and operation conditions.42 Second, an extended triboelectric series of highly deformable and porous fabrics has been obtained through a systematic experimental study.43 The table provides the measured values of effective triboelectric charge density of knitted fabrics made from 21 types of polymeric fibers. Third, we have established theoretical limits of electric charge density and outputs in a contact-mode FTENG by taking consideration of the electric breakdown due to field-induced emission and gas ionization.44

3.1. Fully Verified Theoretical Model of Contact-Mode FTENG

Here the questions we attempted to answer are the following: Since FTENG is working according to the principle of triboelectrification and charge induction, can we quantitatively predict its output performance? An example of contact-mode FTENG42 is shown in Figure 4a. The dielectric layer, with a thickness of d and relative permittivity of ε_r, is stacked face to the top fabric electrode 1. Electrodes 1 and 2 are connected with an external resistor R. The top electrode 1 periodically moves up and down with a separation distance x. Considering the saturated surface charges, it is reasonable to assume that the triboelectric charges are uniformly distributed on the dielectric layer with negligible decay, and the surface charge density is signified as σ. Considering the charge conservation, Gauss law, closed loop circuit, and Ohm's law, the amount of transferred charges, Q, is expressed as

$$R\frac{dQ}{dt} + \frac{Q}{S\varepsilon_0}(d_0 + x(t)) - \frac{\sigma x(t)}{\varepsilon_0} = 0$$

with the initial conditions

$$Q(t=0) = 0,\ \sigma_2 = \frac{Q}{S}$$

The transferred charges can be analytically expressed by

$$Q(t) = \left[\int_0^t \frac{\sigma x(\tau)}{R\varepsilon_0} e^{\int_0^\tau (d_0 + x(z))/(RS\varepsilon_0)dz}\, d\tau\right] e^{\int_0^t (d_0 + x(\tau))/(RS\varepsilon_0)d\tau} \quad (8)$$

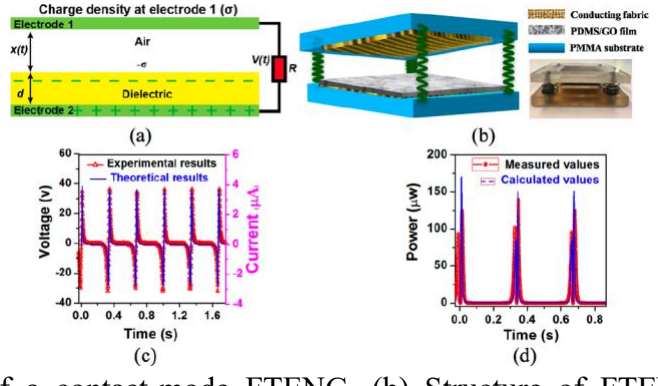

Figure 4. (a) Sketch of a contact-mode FTENG. (b) Structure of FTENG. (c, d) Comparison between experimental and theoretical results of voltage, current, and output power. Reproduced with permission from ref 42. Copyright 2016 Wiley.

With the fabricated FTENG shown Figure 4b, the theoretical model was verified. As shown in Figure 4c,d, the output voltage, current, and power of the FTENG are in an excellent agreement with the corresponding experimental results, without any adjustable parameters.

The effects of the moving speed on output voltage, current, and power were illustrated in three cases; that is, the motion with constant speed, the sinusoidal motion cycles, and the real walking cycles by a human subject. The fully verified theoretical model provides a very powerful tool to guide the design of the device structure, selection of materials, and optimization of performance with respect to the application conditions of TENGs.

3.2. Triboelectric Charge Density of Highly Deformable and Porous Fibrous Materials

In FTENGs, soft, deformable, or porous polymeric materials are utilized, such as textile fabrics made from polytetrafluoro-ethylene (PTFE), polydimethylsiloxane (PDMS), poly(vinyl chloride) (PVC), etc. Our previous theoretical and experimental studies42 have revealed that the surface charge density is the most important factor determining the output performance of such nanogenerators. Generally speaking, material chemical structure and its high-order structures have

direct influences on the number of electric charges. Another effect comes from the morphology of the interactive surface. It is meaningless to compare the absolute charge density values obtained from various tests in the previous works, since the real contact area was not controlled and thus varied for different materials under different testing conditions. More-over, many previous studies did not confirm whether the number of charges of the materials had reached the saturated state, and the testing condition was not illustrated clearly. In addition, materials like textile fabrics are very deformable and porous; thus the previous measurements cannot provide reliable data of absolute charge density of materials despite the existence of the triboelectric series, often obtained from solid materials. Therefore, it is much more desirable to improve the current experimental methods for triboelectric charge density by considering the charge saturation and effects of structural characteristics of the deformable and porous materials, like fabrics.

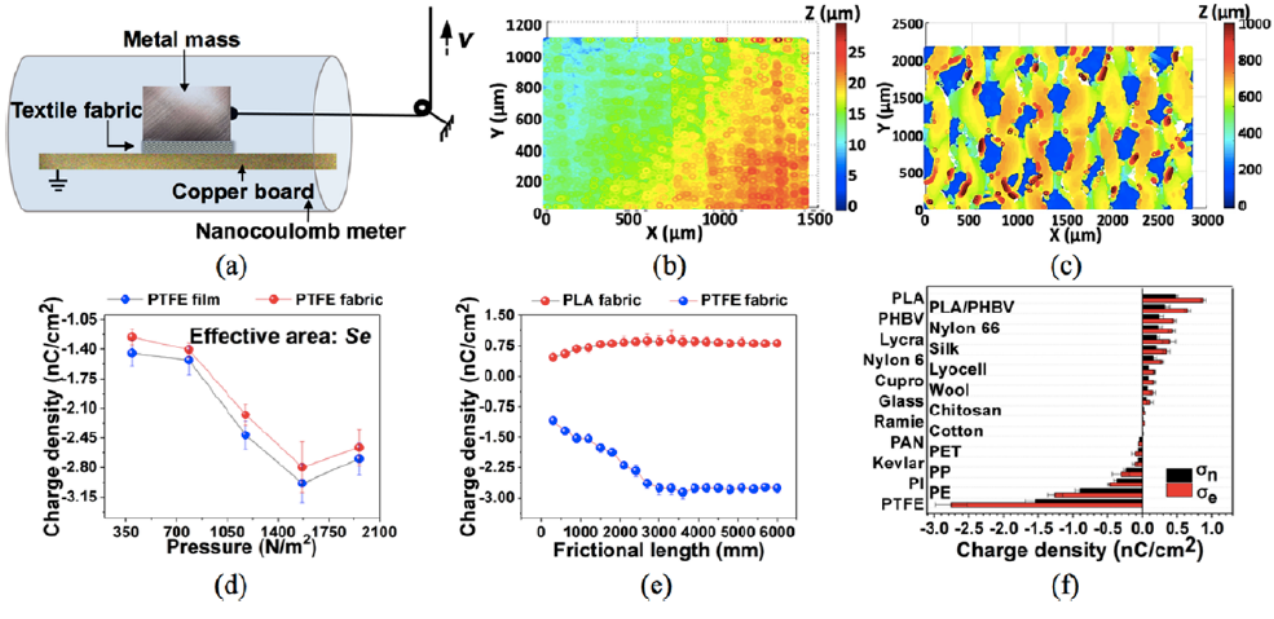

Figure 5. (a) Schematic of triboelectric testing system. (b, c) Microstructures of PTFE film and fabric. (d) Effective charge densities plotted against pressure. (e) Effective charge densities plotted against frictional length. (f) Triboelectric series of fabrics made from 21 types of polymeric fibers. Reproduced with permission from ref 43. Copyright 2018 Elsevier.

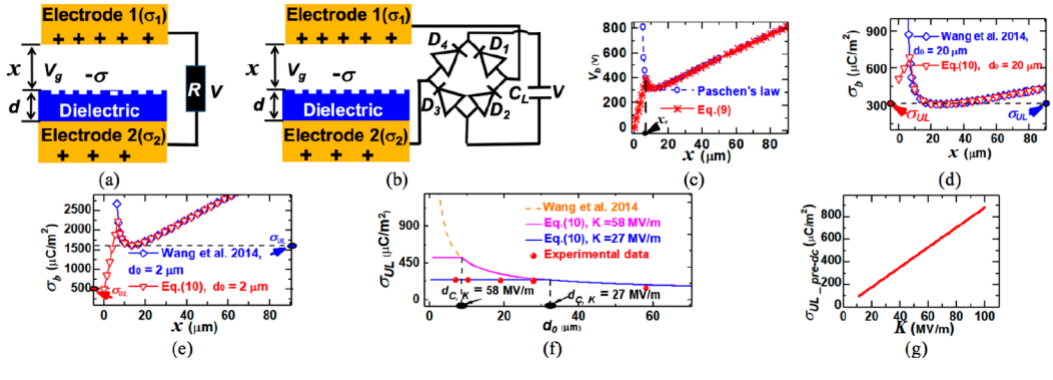

Figure 6. Experimental setup with a resistor (a) and rectifying circuit (b). (c) Theoretical curve of breakdown voltage. (d,e) Maximum surface charge density vs gap distance. (f) Experimental verification. (g) Maximum charge density vs K. Reproduced with permission from ref 44. Copyright 2019 Elsevier.

Sliding contact has been the chosen approach by us to conduct the triboelectrification experiments.43 Several re-searchers previously studied the mechanisms, including an increase in contact area due to interfacial deformation, frictional heating, and direct material transfer. However, many effects were undetermined such as surface morphology and compressibility, variations in experimental methods, the nature of contact, uncertainty as to the transferred charge species, and the effect of charge back-flow.

The electron charge density of porous and deformable textile fabrics made from a range of polymeric fibers was measured by utilizing a lab-made sliding-mode triboelectrification measurement system, as illustrated by Figure 5a. We carefully determined the surface characteristics (Figure 5b,c), charge density as a function of pressure (Figure 5d), and sliding length (Figure 5e), as well as the effects of temperature and friction coefficient. After the triboelectrification process reached its saturation under the fabric densification pressure, the effective contact area will not be influenced by the variation in porosity of fabric structure due to pressure; the measured charge density of fabrics can regarded as the effective charge density by taking into account of the effective contact area. An extended table of effective charge density was compiled covering fabrics made from 21 types of polymer fibers, including new fibers like poly(3-hydroxybutyrate-co-3-hydrox-yvalerate), polylactide, Lyocell, and cuprammonium (Figure 5f).

3.3. Theoretical Upper Limits of Output of FTENG

The theoretical model in section 3.1 works very well provided there is no air-breakdown in the gap of the FTENG. However, the strong electric field in the surrounding media may result in gas ionization breakdown, where the charge density will drop dramatically without control. The breakdown voltage due to gas ionization can be described by Paschen's law. In addition, the strong electric field may induce more charges on the surface. The field emission induced breakdown is eminent when the gap distance is small, that is, several micrometers or below. Therefore, we must consider the two phenomena in a holistic manner.44 Figure 6c shows that in view of both the breakdown voltage, Vb, can be described as follows:

$$V_b = \begin{cases} Kx & 0 < x \le x_c \\ \dfrac{Bpx}{\ln(px) + C} & x > x_c \end{cases} \quad (9)$$

where K is the threshold electric field required for field emission, which is related to the work function of the cathode, geometry of the surface, pressure, and composition of the gas. In practice,

it is normally obtained as a fitting constant. The constants in the second equation are given by Paschen's law.45

Because the voltage in the gap is always smaller than the breakdown voltage, the maximum surface charge density of a working FTENG can be given as the lowest value determined by

$$\sigma_{max} = \min(F_{SC}) \qquad (10)$$

where

$$F_{SC} = \begin{cases} K\varepsilon_0 \dfrac{d_0 + x}{d_0} & \text{for } 0 < x \le x_c \\ \dfrac{Bp\varepsilon_0}{\ln(px) + C} \dfrac{d_0 + x}{d_0} & \text{for } x_c \le x \le x_{max} \end{cases}$$

and when the FTENG is under the short-circuit condition.

To verify the theoretical analysis, we used a FTENG comprising a PDMS thin film and conductive aramid paper as electrodes with external resistor or rectifying bridge (Figure 6a,b). The upper limit of transferred charges between electrodes varies significantly with the thickness of the dielectric layer as shown in Figure 6d,e. It was found to be a linear function of the area of the interactive surfaces, relative dielectric constant, and threshold electric field required for field emission (Figure 6g). Figure 6f depicts that the prediction is in good agreement with the experimental ones. Based on the upper limits, the outputs of a given FTENG have been derived theoretically.

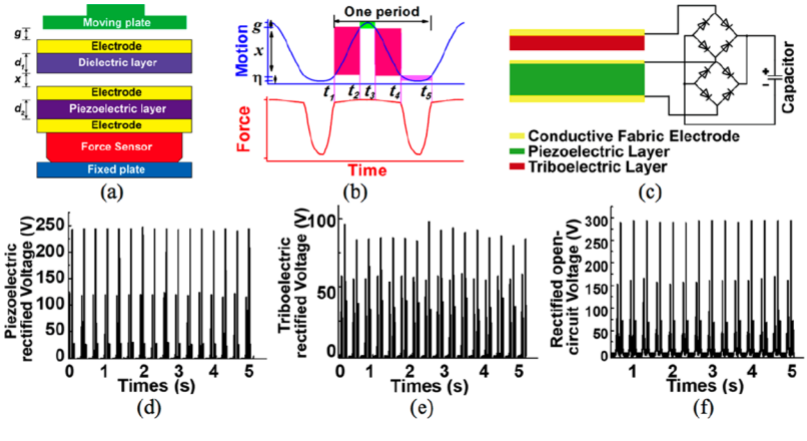

Figure 7. (a) Schematic of the device. (b) Motion and force as a function of time. (c) Equivalent circuit with two full-wave bridge circuits and a capacitor. (d−f) Rectified output voltage of FPENG, FTENG, and hybrid generator, respectively. Reproduced with permission from ref 36. Copyright 2017 Wiley.

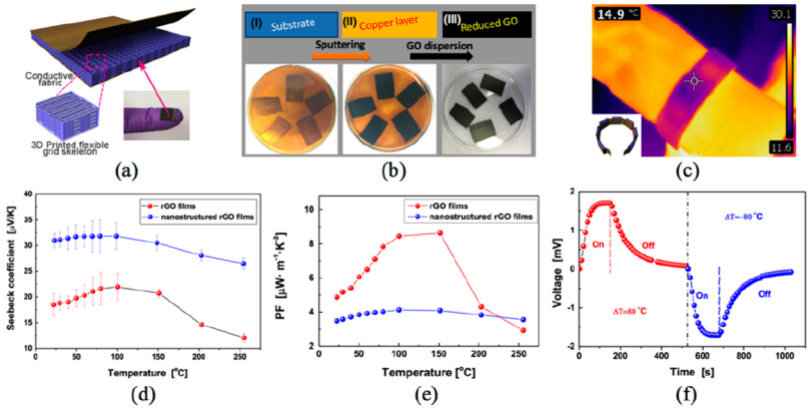

Figure 8. (a) Three-dimensional printed flexible FTEG with a 3D grid skeleton and conductive fabric. (b) Processes for rGO. (c) Infrared image of band-type wearable FTEG. (d−f) Seebeck coefficient, power factor, and voltage of the FTEG. Reproduced with permission from ref 47. Copyright 2018 Elsevier.

4. FIBER-BASED HYBRID NANOGENERATOR

Hybrid generators with cascaded piezoelectric and triboelectric units have advantages when working in contact-mode for applications such as the large area of floor coverings like run-ways and carpets, as well as foot-mounted wearable electronic systems, because of short vertical displacement and easy integration. However, most published reports are experimental investigations only, often with varied and contradictory results. No theoretical treatment had been proposed on the charge generation and transfer processes as well as power output of such hybrid generators. Therefore, we attempted to address the key questions, including the following: Is there any synergistic effect between the two units? If yes, how large is the synergistic effect of hybridization with respect to the individual effect? How can one illustrate the working principle and predict the output?

4.1. Mechanism of Hybrid Generators and Synergy

For the first time, a theoretical analysis of the contact-mode hybrid generator with cascaded piezoelectric and triboelectric units was presented by us to illustrate the working mechanism and to describe the relationships among transfer charges, voltage, current, and average output power in terms of materials properties, device structural parameters, harvesting, and operational conditions.35 The schematic diagram of the hybrid generator is shown in Figure 7a. Subjected to an approximate sinusoidal load, the two cascaded units, namely, the piezoelectric unit and triboelectric unit, go through a sequence of deformation and activation (Figure 7b). Connected with two fully rectifying bridges, the multistage charge generation and transfer process is illustrated in Figure 8c.

4.2. Synergy between FPENG and FTENG Units

The hybrid generators were fabricated by using P(VDFTrFE)/Ag composite fabric as the piezoelectric layer, a PDMS/graphite composite as the triboelectric layer, and three fabric electrodes in a cascaded structure. In the piezoelectric layer, Ag nanowires were used to enhance piezoelectricity and electric conductivity of P(VDF-TrFE) nanofibers and to achieve a high dielectric constant and low dielectric loss. Graphite nanoparticles were utilized to increase the dielectric constant of the triboelectric layer. The output voltage and current were measured for individual units (Figure 7d,e) and the hybrid generator (Figure 7f). Since there is a phase difference between the output signals from the two units, two rectifying bridges should be employed to avoid the cancel-out of signal and reduction of the output, as demonstrated in Figure 7c. The output power of the hybrid generator was found to be the sum of those of two individual units. This way, we did not detect either positive or negative synergy between the two individual units.

4.3. Transferred Charges and Output of Hybrid Generators

As the working states for FTENG and FPENG units are completely decoupled, by using a similar analysis of circuit, the output current, voltage, and power are deduced from the transferred charges. Considering the initial conditions, namely,

$$\begin{cases} Q_1(t=0) = 0 \\ Q_2(t=0) = 0 \\ Q_3(t=0) = \sigma S \end{cases}$$

where Q1, Q2, and Q3 are the charges on electrodes 1, 2, and 3. The transferred charges are derived for different phases, namely,

$$\begin{cases} Q_1(t) = \sigma S - \sigma S \exp\left(-\dfrac{1}{R_1 S \varepsilon_0}\left(\dfrac{d_1}{\varepsilon_{r1}} t + \displaystyle\int_0^t x(t)\,\mathrm{d}t\right)\right) \\ \qquad - \dfrac{\sigma d_1}{R_1 \varepsilon_0 \varepsilon_{r1}} \exp\left(-\dfrac{1}{R_1 S \varepsilon_0}\left(\dfrac{d_1}{\varepsilon_{r1}} t + \displaystyle\int_0^t x(t)\,\mathrm{d}t\right)\right) \times \\ \qquad \displaystyle\int_0^t \exp\left(\dfrac{1}{R_1 S \varepsilon_0}\left(\dfrac{d_1}{\varepsilon_{r1}} z + \int_0^z x(z)\,\mathrm{d}z\right)\right)\mathrm{d}z \quad (\Delta t_2, \Delta t_4) \\ Q_2(t) = 0 \end{cases} \tag{11}$$

and

$$\begin{cases} Q_1(t) = 0 \\ Q_2(t) = d_{31} Y_c w s_1(t) + d_{33} Y_c w l s_3(t) \quad (\Delta t_1, \Delta t_3) \end{cases} \tag{12}$$

where the σ is surface charge density induced by triboelectric effect, d1 is the thickness of electrode 1 and S contact area of electrode 1, ε_0 and ε_{r1} are the air permittivity and relative permittivity, and R1 is the external resistance. Other parameters are defined in the same way as in eq 5.

5. FIBER-BASED THERMOELECTRIC NANOGENERATOR (FTEG)

FTEGs are a spanking new type of solid-state thermoelectric device that are large-sized, three-dimensionally deformable, lightweight, and comfortable. FTEGs are fiber-structured stationary energy harvesting devices working according to the Seebeck effect, which describes the movement of electric charges (electrons or holes) in a thermoelectric material due to temperature difference. Detailed descriptions have been given in a review paper.46 Their manufacturing can be made cost-effective by deploying low-temperature industrial processes. FTEGs have demonstrated abundant possibilities in applications such as large-area waste heat recovery and wearable or portable electronic systems. Their aptitudes as refrigerating devices are yet to be explored for microclimate control by personalized smart clothing systems.

5.1. New TE Materials for Wearable FTEGs

Despite of all the promises, the challenges are great and numerous to realize fiber-based thermoelectric energy conversion systems based on FTEGs. Appropriate TE materials should have a high Seebeck coefficient and power factor, possess high electric conductivity as well as low thermal conductivity, and be processable at low or room temperature using cost-effective processes. TE materials reported in the literature include inorganic (i.e., Bi−Te alloys), organic (i.e., PEDOT:PSS and PANI), and graphene or polymer composite materials. At present, few suitable, safe, and flexible thermoelectric (TE) materials with excellent TE properties can be applied to clothing-type polymer fibers, whose operational temperatures are normally below 300 degrees centigrade. A detailed review on principle, materials, devices, characterization, and applications was given in ref 46. Graphene is a stable and safe material compared with many inorganic and organic TE materials. For being used as a TE material, opening of graphene's band gap while maintaining its high electric conductivity is necessary. In order to achieve this, by employing a synchronous reduction and assembly approach, two-dimensional reduced graphene oxide films were prepared. The continuous films exhibited a low in-plane thermal conductivity of 2.96 W/m·K and cross-plane one of 0.30 W/ m·K at room temperature, while they displayed a high in-plane electrical conductivity of 1.43 Å~ 104 S/m.47 The high longitudinal carrier mobility of the connected lattice domains is attributed to the high electrical conductivity. The enhanced scattering of phonons in the defects and the boundary reduces the mean phonon free path to a large extent and hence significantly lowers the thermal conductivity. Moreover, using the same strategy, the large-area films can be easily formed and anchored on three-dimensional surfaces. Meanwhile, composites containing inorganic TE particles and conductive polymers have been investigated by us for disperse printing or coating. One example is p-type Bi2Te3/PEDOT:PSS thermoelectric composite, whose Seebeck coefficient is slightly higher than that of pure Bi2Te3 at room temperature, representing the highest value for BixTey/PEDOT:PSS composites reported so far. Theoretical treatments of these materials are ongoing and will be reported in the future.

5.2. Fabrication of Ftegs

FTEGs were prepared by assembling reduced graphene oxide films on 3D printed polydimethylsiloxane grids, as shown in Figure 8a,b. A wristband was assembled by using seven flexible thermoelectric generator units connected in series. It yielded a maximum power density of

6.3 μW/g at 15 °C. The fabrication method of synchronous reduction and assembly on 3D printed grids is conducted at room temperature in solution and thus can be easily scaled up for production of flexible and wearable energy harvesting systems.

Since the low voltage from the FTEG cannot be directly used to power electronic devices, energy conversion control circuits are mandatory to convert the voltage to the required level. Furthermore, in order to extract all available power from the FTEG, a maximum power point tracking (MPPT) algorithm needs to be included. Inductive-based48 energy conversion control circuits have been developed using a pulse transformer and fully integrated capacitive-based circuit. To further improve the power conversion efficiency with wide temperature range, reconfigurable array based circuits were reported, whose operation differs from the conventional circuits as the MPPT is no longer achieved by impedance matching.49

6. SUMMARY AND PERSPECTIVE

In the last five years, we have successfully developed a number of new models for fiber-based piezoelectric, triboelectric, and hybrid generators for the prediction of their output performance in terms of materials, device structure, harvesting circuits, and storage. We have identified the theoretical upper limits of output for contact-mode FTENG by considering the electric breakdown due to field-induced emission and gas ionization. We have setup an experimental platform for reliable tribo-electric charge measurement of highly deformable and porous materials like fabrics. An extended triboelectric series has been reported including 21 types of commercial and new fibers. Based upon the findings, we have made significant improvements of the performance of these devices.

A class of flexible thermoelectric materials has been explored and exhibited high performance from fiber-based thermo-electric generators made from low-temperature and cost-effective processes. They have been used for fabricating fiber-base thermoelectric generators, key devices for great potential applications such as powering wearable microelectronic systems, active microclimate regulating systems, and waste thermal energy harvesting. Although we are closer to it than ever before, our investigations will continue and expand50 in order to reach the final goal that the wearable systems can work for us anywhere at any time.

ACKNOWLEDGMENTS

The work has been supported by Research Grants Council, Hong Kong, China (Nos. 525113, 15215214, 15204715, and 15200916), and Hong Kong Polytechnic University (No. 1-BBA3).

REFERENCES

[1] Tao, X. M. Handbook of smart textiles; Springer: Singapore, 2015.
[2] Zeng, W.; Shu, L.; Li, Q.; Chen, S.; Wang, F.; Tao, X. M. Fiber-based wearable electronics: a review of materials, fabrication, devices, and applications. Adv. Mater. 2014, 26, 5310−5336.
[3] Yi, W.; Wang, Y.; Wang, G.; Tao, X. M. Investigation of carbon black/silicone elastomer/dimethylsilicone oil composites for flexible strain sensors. Polym. Test. 2012, 31, 677−684.
[4] Ying, D.; Tao, X. M.; Zheng, W.; Wang, G. Fabric strain sensor integrated with looped polymeric optical fiber with large angled V-shaped notches. Smart Mater. Struct. 2013, 22, No. 015004.
[5] Xue, P.; Wang, J.; Tao, X. M. Flexible textile strain sensors from polypyrrole-coated XLA elastic fibers. High Perform. Polym. 2014, 26, 364−370.
[6] Wang, F.; Zhu, B.; Shu, L.; Tao, X. M. Flexible pressure sensors for smart protective clothing against impact loading. Smart Mater. Struct. 2014, 23, No. 015001.
[7] Zhang, H.; Tao, X. M. A single-layer stitched electrotextile as flexible pressure mapping sensor. J. Text. Inst. 2012, 103, 1151−1159.
[8] Wang, F.; Liu, S.; Shu, L.; Tao, X. M. Low-dimensional carbon based sensors and sensing network for wearable health and environmental monitoring. Carbon 2017, 121, 353−367.
[9] Zhang, Z. F.; Tao, X. M.; Zhang, H. P.; Zhu, B. Soft fiber optic sensors for precision measurement of shear stress and pressure. IEEE Sens. J. 2013, 13, 1478−1482.
[10] Zhang, Z. F.; Tao, X. M. Intrinsic temperature sensitivity of fiber bragg gratings in PMMA-based optical fibers. IEEE Photonics Technol. Lett. 2013, 25, 310−312.
[11] Li, Q.; Zhang, L. N.; Tao, X. M.; Ding, X. Review of flexible temperature sensing networks for wearable physiological monitoring. Adv. Healthcare Mater. 2017, 6, 1601371.
[12] Li, Q.; Chen, H.; Ran, Z. Y.; Zhang, L. N.; Xiang, R. F.; Tao, X. M.; Ding, X.; Wang, X. Full fabric sensing network with large deformation for continuous detection of skin temperature. Smart Mater. Struct. 2018, 27, 105017.
[13] Zhang, Z. F.; Tao, X. M. Synergetic effects of humidity and temperature on PMMA based fiber Bragg gratings. J. Lightwave Technol. 2012, 30, 841−845.
[14] Wang, D. H.; Hu, Y.; Zhao, J. J.; Zeng, L. L.; Tao, X. M.; Chen, W. Holey reduced graphene oxide nanosheets for high performance room temperature gas sensing. J. Mater. Chem. A 2014, 2, 17415− 17420.
[15] Wang, D. H.; Gu, W.; Zhang, Y. W.; Hu, Y.; Zhang, T.; Tao, X. M.; Chen, W. Novel C-rich carbon nitride for room temperature NO2 gas sensors. RSC Adv. 2014, 4, 18003−18006.
[16] Li, Q.; Tao, X. M. Three-dimensionally deformable, highly stretchable, permeable, durable and washable fabric circuit boards. Proc. R. Soc. London, Ser. A 2014, 470, 20140472.
[17] Shen, J.; Chui, C. H.; Tao, X. M. Luminous fabric devices for wearable low-level light therapy. Biomed. Opt. Express 2013, 4, 2925− 2937.
[18] Shen, J.; Tao, X. M.; Ying, D. Q.; Hui, C. Y.; Wang, G. F. Light-emitting fabrics integrated with structured polymer optical fibers treated with an infrared CO2 laser. Text. Res. J. 2013, 83, 730−739.
[19] Pun, C.F. J.; Liu, Z. Y.; Tse, M. L. V.; Cheng, X.; Tao, X. M.; Tam, H. Y. Side-illumination fluorescence dye-doped-clad pmma-core polymer optical fiber: potential intrinsic light source for biosensing. IEEE Photonics Technol. Lett. 2012, 24, 960−962.
[20] Lu, C.; Yang, Y.; Wang, J.; Fu, R. P.; Zhao, X. X.; Zhao, L.; Ming, Y.; Hu, Y.; Lin, H. Z.; Tao, X. M.; Li, Y. L.; Chen, W. High-performance graphdiyne-based electrochemical actuators. Nat. Commun. 2018, 9, 752.
[21] Hu, Y.; Lan, T.; Wu, G.; Zhu, Z. C.; Tao, X. M.; Chen, W. Novel electromechanical actuation based on a spongy graphene paper. Chem. Commun. 2014, 50, 4951−4954.

[22] Shu, L.; Tao, X. M.; Feng, D. D. A new approach for readout of resistive sensor arrays for wearable electronic applications. IEEE Sens. J. 2015, 15, 442−452.
[23] Shu, L.; Hua, T.; Wang, Y. Y.; Li, Q. A.; Feng, D. D.; Tao, X. M. In-shoe plantar pressure measurement and analysis system based on fabric pressure sensing array. IEEE Trans. Inf. Technol. Biomed. 2010, 14, 767−775.
[24] Wang, X.; Tao, X. M. Continuous monitoring and modeling contractility of skeletal muscles in motion: a review. Med. Res. Archives 2018, 6, 1797.
[25] Wang, X.; Tao, X. M.; So, R. C. H. A bio-mechanical model for elbow isokinetic and isotonic flexions. Sci. Rep. 2017, 7, 8919.
[26] Wang, X.; Tao, X. M.; So, R. C. H.; Shu, L.; Yang, B.; Li, Y. Monitoring elbow isometric contraction by novel wearable fabric sensing device. Smart Mater. Struct. 2016, 25, 125022.
[27] Xiong, Y.; Tao, X. M. Compression garments for medical therapy and sports. Polymers 2018, 10, 663.
[28] Zheng, W.; Tao, X. M.; Zhu, B.; Wang, G. F.; Hui, C. Y. Fabrication and evaluation of a notched polymer optical fiber fabric strain sensor and its application in human respiration monitoring. Text. Res. J. 2014, 84, 1791−1802.
[29] Sun, J. F.; Huang, Y.; Sea, Y. N. S.; Xue, Q.; Wang, Z. F.; Zhu, M. S.; Li, H. F.; Tao, X. M.; Zhi, C. Y.; Hu, H. Recent progress of fiber-shaped asymmetric supercapacitors. Mater. Today Energy 2017, 5, 1−14.
[30] Gao, L.; Song, J.; Surjadi, J. U.; Cao, K.; Han, Y.; Sun, D.; Tao, X. M.; Lu, Y. Graphene-bridged multifunctional flexible fiber supercapacitor with high energy density. ACS Appl. Mater. Interfaces 2018, 10, 28597−28607.
[31] Sun, J.; Huang, Y.; Fu, C.; Huang, Y.; Zhu, M.; Tao, X. M.; Zhi, C.; Hu, H. A high performance fiber-shaped PEDOT@ MnO 2//C@ Fe 3 O 4 asymmetric supercapacitor for wearable electronics. J. Mater. Chem. A 2016, 4, 14877−14883.
[32] Song, J.; Chen, Y. J.; Cao, K.; Lu, Y.; Xin, J. H.; Tao, X. M. Fully controllable design and fabrication of three-dimensional lattice supercapacitors. ACS Appl. Mater. Interfaces 2018, 10 (46), 39839− 39850.
[33] Wang, Y.; Su, S. Y.; Cai, L. J.; Qiu, B. C.; Yang, C.; Tao, X. M.; Chai, Y. Hierarchical supercapacitor electrodes based on metallized glass fiber for ultrahigh areal capacitance. Energy Storage Mater. 2018, DOI: 10.1016/j.ensm.2018.11.018.
[34] Liu, Y.; Hu, Y.; Zhao, J.; Wu, G.; Tao, X. M.; Chen, W. Self-powered piezoionic strain sensor toward the monitoring of human activities. Small 2016, 12, 5074−5080.
[35] Zeng, W.; Tao, X. M.; Chen, S.; Shang, S. M.; Chan, H.L. W.; Choy, S. H. Highly durable all-fiber nanogenerator for mechanical energy harvesting. Energy Environ. Sci. 2013, 6, 2631−2638.
[36] Chen, S.; Tao, X. M.; Zeng, W.; Yang, B.; Shang, S. M. Quantifying energy harvested from contact-mode hybrid nano-generators with cascaded piezoelectric and triboelectric units. Adv. Energy Mater. 2017, 7, 1601569.
[37] Song, J.; Yang, B.; Zeng, W.; Peng, Z.; Lin, S.; Li, J.; Tao, X. M. Highly flexible, large-area, and facile textile-based hybrid nano-generator with cascaded piezoelectric and triboelectric units for mechanical energy harvesting. Adv. Mater. Technol. 2018, 3, 1800016.
[38] Zhong, J. W.; Zhang, Y.; Zhong, Q.; Hu, Q.; Hu, B.; Wang, Z. L.; Zhou, J. Fiber-based Generator for wearable electronics and mobile medication. ACS Nano 2014, 8, 6273−6280.
[39] Dong, K.; Deng, J.; Zi, Y.; Wang, Y. C.; Xu, C.; Zou, H.; Ding, W.; Dai, Y.; Gu, B.; Sun, B.; Wang, Z. L. 3D orthogonal woven triboelectric nanogenerator for effective biomechanical energy harvesting and as self-powered active motion sensors. Adv. Mater. 2017, 29, 1702648.

[40] Dong, K.; Deng, J.; Ding, W.; Wang, A. C.; Wang, P.; Cheng, C.; Wang, Y.; Jin, L.; Gu, B.; Wang, Z. L.; Sun, B. Versatile core− sheath yarn for sustainable biomechanical energy harvesting and real-time human-interactive sensing. Adv. Energy Mater. 2018, 8, 1801114.
[41] Song, J.; Gao, L.; Tao, X. M.; Li, L. Ultra-flexible and large-area textile-based triboelectric nanogenerators with a sandpaper-induced surface microstructure. Materials 2018, 11, 2120.
[42] Yang, B.; Zeng, W.; Peng, Z. H.; Liu, S. R.; Chen, K.; Tao, X. M. A fully verified theoretical analysis of contact-mode triboelectric nanogenerators as a wearable power source. Adv. Energy Mater. 2016, 6, 1600505.
[43] Liu, S.; Zheng, W.; Yang, B.; Tao, X. M. Triboelectric charge density of porous and deformable fabrics made from polymer fibers. Nano Energy 2018, 53, 383−390.
[44] Yang, B.; Tao, X. M.; Peng, Z. H. Upper limits for output performance of contact-mode triboelectric nanogenerator systems. Nano Energy 2019, 57, 66−73.
[45] Wang, S. H.; Xie, Y. N.; Niu, S. M.; Lin, L.; Liu, C.; Zhou, Y. S.; Wang, Z. L. Maximum surface charge density for triboelectric nanogenerators achieved by ionized-air injection: methodology and theoretical understanding. Adv. Mater. 2014, 26, 6720−6728.
[46] Zhang, L. S.; Lin, S. P.; Hua, T.; Huang, B. L.; Liu, S. R.; Tao, X. M. Fiber-based thermoelectric generators: materials, device structures, fabrication, characterization, and applications. Adv. Energy Mater. 2018, 8, 1700524.
[47] Zeng, W.; Tao, X. M.; Lin, S. P.; Lee, C.; Shi, D. L.; Lam, K. H.; Huang, B. L.; Wang, Q. M.; Zhao, Y. Defect-engineered reduced graphene oxide sheets with high electric conductivity and controlled thermal conductivity for soft and flexible wearable thermoelectric generators. Nano Energy 2018, 54, 163−174.
[48] Teh, Y. K.; Mok, P. K. T. Design of transformer-based boost converter for high internal resistance energy harvesting sources with 21 mv self-startup voltage and 74% power efficiency. IEEE J. Solid-State Circuits 2014, 49, 2694−2704.
[49] Wan, Q. P.; Teh, Y. K.; Gao, Y.; Mok, P. K. T. Analysis and design of a thermoelectric energy harvesting system with reconfigurable array of thermoelectric generators for iot applications. IEEE T. Circuits-I. 2017, 64, 2346−2358.
[50] Xie, C.; Mak, C. H.; Tao, X. M.; Yan, F. Photodetectors based on two-dimensional layered materials beyond graphene. Adv. Funct. Mater. 2017, 27, 1603886.